

1 **Effects of perpendicular diffusion on energetic particles accelerated by the**
2 **interplanetary coronal mass ejection shock**

3 Y. Wang^{1,2}, G. Qin¹ and M. Zhang³

4 Yang Wang, ywang@spaceweather.ac.cn; Gang Qin, gqin@spaceweather.ac.cn;

5 Ming Zhang, mzhang@fit.edu

6 Received _____; accepted _____

¹State Key Laboratory of Space Weather, Center for Space Science and Applied Research,
Chinese Academy of Sciences, Beijing 100190, China

²College of Earth Sciences, Graduate University of Chinese Academy of Sciences, Beijing
100049, China

³Department of Physics and Space Sciences, Florida Institute of Technology, Melbourne,
Florida 32901, USA

ABSTRACT

7
8 In this work, based on a numerical solution of the focused transport equation, we
obtained the intensity and anisotropy time profiles of solar energetic particles (SEP)
accelerated by an interplanetary shock in the three-dimensional Parker magnetic field.
The shock is treated as a moving source of energetic particles with an assumed particle
distribution function. We computed the time profiles of particle flux and anisotropy as
measured by an observer at 1 AU, equatorial plane and various longitudes with respect
to the shock propagation direction. With perpendicular diffusion, energetic particles
can cross magnetic field lines. Particles may be detected before the observer's field
line is connected to the shock. After the observer's field line breaks from the shock
front, the observer still can see more particles are injected into its field line. Our sim-
ulations show that the particle onset time, peak time, peak intensity, decay rate and
duration of SEP event could be significantly influenced by the effect of perpendicular
diffusion. The anisotropy with perpendicular diffusion is almost the same as that with-
out perpendicular diffusion, but there is an obvious difference at the moment when the
observer's field line begins to be connected to the shock.

9 *Subject headings:* Sun: energetic particles — Sun: shock — Sun: magnetic field

1. Introduction

Solar energetic particle events can roughly be divided into two categories: impulsive events and gradual events. The impulsive events, with the characteristics of short duration and low intensity, are produced by solar flares. Gradual events, usually having high intensity and lasting longer, are related to the shocks driven by coronal mass ejections (CMEs). Even though CME shocks cover a large range of solar longitude and latitude, the source of SEP is not uniformly distributed in the corona. Depending on its angular location, an observer in the interplanetary space may or may not be directly connected to the source by the magnetic field. Simultaneous multi-spacecraft observations by e.g. STEREO, clearly show huge difference of SEP time profiles at different longitudes (Liu et al. 2011).

Generally, there are two major approaches to model SEP shock acceleration: Heras et al. (1992, 1995); Kallenrode & Wibberenz (1997); Lario et al. (1998); Ng et al. (1999); Kallenrode (2001) injected SEPs at the shock with an assumed injection strength, while a few other studies also include the acceleration of SEPs by CME shocks (Lee 1983; Gordon et al. 1999; Zank et al. 2000; Li et al. 2003; Rice et al. 2003; Sokolov et al. 2004; Lee 2005). In these models, three important effects of acceleration and propagation mechanisms have been involved. The first effect is the acceleration process by the CME-driven shock. Zank et al. (2000) provided an onion shell model based on the first-order Fermi acceleration mechanism. They used a one-dimensional hydrodynamic code to describe the evolution of the CME-driven shock in the Parker model of interplanetary magnetic field (IMF). Wave excitation by streaming energetic particles produced at shock is included in the model, and the diffusion coefficient is calculated from a wave energy equation. However, the model is only applicable to extremely strong shocks, due to the use of Bohm diffusion coefficient. Their simulation results reveal that the maximum energy can go up to the order of GeV when shock is near the Sun. Rice et al. (2003) extended Zank et al. (2000) model so that it is applicable to shock waves of arbitrary strengths. The second effect is the

35 scattering by waves generated by the streaming particles. Ng et al. (1999, 2001, 2003) presented
36 a model of particle transport including streaming proton generated Alfvén waves, in which the
37 shock acceleration is represented by a moving SEPs source, and the particle diffusion coefficients
38 are expressed by wave intensity and wave growth rates. Their simulation results agree well with
39 the observed evolution of spectral slope and abundance ratios of heavy ions in gradual SEP events,
40 and they show that the wave amplification plays a very important role in SEP transport process.
41 The third effect is the realistic geometry of CME and its shock. Magnetic field lines can be
42 distorted by the CME shock, which is important for the acceleration and transport of SEPs (Zank
43 et al. 2006). Sokolov et al. (2004) simulated particle acceleration and transport as the CME shock
44 wave evolves with radial distance from 4 to 30 R_{\odot} from the sun. With numerical solution of a
45 fully three-dimensional MHD model, the realistic structures of CME and its shock can be derived.
46 Their simulation results demonstrate that the diffusive shock acceleration theory can account for
47 the increase of high energy protons (hundreds of MeV) during solar eruptions.

48 In all these previous works, it was generally assumed that particles are transported only
49 along the magnetic field lines. This assumption was justified, if, according to an early theory
50 (Jokipii 1966), perpendicular diffusion coefficient is generally much smaller than the parallel one.
51 However, perpendicular diffusion coefficients change significantly from event to event. For some
52 events, observation results show that the perpendicular diffusion coefficients could be comparable
53 to the parallel ones (Dwyer et al. 1997; Zhang et al. 2003). This phenomenon has also been
54 obtained by the test particle simulations that included non-linear effects of magnetic turbulence
55 (Qin et al. 2002a,b; Qin 2002). Later on, Matthaeus et al. (2003); Shalchi et al. (2004); Bieber
56 et al. (2004), and Qin (2007) developed a nonlinear guiding center diffusion theory and found a
57 better agreement with numerical simulations and observations. Furthermore, new observations
58 from STEREO show that even some impulsive ^3He rich events (Wiedenbeck et al. 2010) can cover
59 a much wider longitudinal extent than the width of solar flare, indicating that there is significant
60 perpendicular particle transport.

85 2009)

$$\frac{\partial f}{\partial t} - \nabla \cdot (\mathbf{\kappa}_{\perp} \cdot \nabla f) + (v\mu \hat{\mathbf{b}} + \mathbf{V}^{sw}) \cdot \nabla f + \frac{dp}{dt} \frac{\partial f}{\partial p} + \frac{d\mu}{dt} \frac{\partial f}{\partial \mu} - \frac{\partial}{\partial \mu} \left(D_{\mu\mu} \frac{\partial f}{\partial \mu} \right) = 0, \quad (1)$$

86 where $f(\mathbf{x}, \mu, p, t)$ is the gyrophase-averaged distribution function, \mathbf{x} is the position in a
 87 non-rotating heliographic coordinate system, $\hat{\mathbf{b}}$ is a unit vector along the local magnetic field, p is
 88 the particle momentum in the solar wind frame, μ is the particle pitch-angle cosine in the solar
 89 wind frame, t is the time, v is the particle speed, \mathbf{V}^{sw} is the solar wind velocity. The adiabatic
 90 cooling effect term, dp/dt , is written as (Skilling 1971; Qin et al. 2004)

$$\frac{dp}{dt} = -p \left[\frac{1 - \mu^2}{2} \left(\nabla \cdot \mathbf{V}^{sw} - \hat{\mathbf{b}} \hat{\mathbf{b}} : \nabla \mathbf{V}^{sw} \right) + \mu^2 \hat{\mathbf{b}} \hat{\mathbf{b}} : \nabla \mathbf{V}^{sw} \right], \quad (2)$$

91 The time evolution of μ is written as (Roelof 1969; Isenberg 1997; Kota & Jokipii 1995)

$$\frac{d\mu}{dt} = \frac{1 - \mu^2}{2} \left[-\frac{v}{L} + \mu \left(\nabla \cdot \mathbf{V}^{sw} - 3 \hat{\mathbf{b}} \hat{\mathbf{b}} : \nabla \mathbf{V}^{sw} \right) \right], \quad (3)$$

92 where the magnetic focusing length L is a derivative of the IMF strength B $L = \left(\hat{\mathbf{b}} \cdot \nabla \ln B \right)^{-1}$. The
 93 relationship of the parallel mean free path (mfp) λ_{\parallel} and $D_{\mu\mu}$ is written as (Jokipii 1966; Earl 1974)

$$\lambda_{\parallel} = \frac{3v}{8} \int_{-1}^{+1} \frac{(1 - \mu^2)^2}{D_{\mu\mu}} d\mu, \quad (4)$$

94 The radial mean free path λ_r is assumed to be a constant throughout heliosphere and the parallel
 95 mean free path λ_{\parallel} is given by (Bieber et al. 1994)

$$\lambda_r = \lambda_{\parallel} \cos^2 \psi, \quad (5)$$

96 where ψ is the angle between the radial direction and the local magnetic field direction. We follow
 97 the model of pitch angle diffusion coefficient from Beeck & Wibberenz (1986)

$$D_{\mu\mu}^r = D_{\mu\mu} / \cos^2 \psi = D_0 v p^{-2/3} \left\{ |\mu|^{q-1} + h \right\} (1 - \mu^2), \quad (6)$$

98 where the constant D_0 is used to control the magnetic field fluctuations level. The constant q is
 99 chosen $q = 5/3$ for a Kolmogorov spectrum type of the spectral power density of magnetic field

100 turbulence in the inertial range. The constant h comes from the non-linear effects of magnetic
 101 turbulence on pitch angle diffusion at $\mu = 0$ (Qin & Shalchi 2009). We have chosen a relatively
 102 large value of $h = 0.2$, but it does not significantly affect the particle mean free path.

103 The perpendicular diffusion coefficient is assumed to be

$$\kappa_{\perp} = \kappa_0 \left(\frac{v}{c}\right) \left(\frac{p}{1\text{GeV}c^{-1}}\right)^{2/3} \left(\frac{B_e}{B}\right) (\mathbf{I} - \hat{\mathbf{b}}\hat{\mathbf{b}}), \quad (7)$$

104 where B_e is the magnetic field strength at the Earth, and B is the magnetic field strength at the
 105 location of a particle. \mathbf{I} is a unit tensor. κ_{\perp} is set to be independent of μ for simplicity, because any
 106 of its μ dependence will be averaged out through a much faster pitch angle diffusion.

107 The anisotropy A is defined as:

$$A = \frac{3 \int_{-1}^1 f(\mu)\mu d\mu}{\int_{-1}^1 f(\mu)d\mu} \quad (8)$$

108 where $f(\mu)$ is the differential flux.

109 We use a partial spherical shell to model the cross section of CME shock which is shown in
 110 Figure 1. In the figure, the shock front is indicated by the dashed arc line, and the shock nose
 111 is indicated by the dashed-arrow radial line passing through the center of the shock. The small
 112 circles, which are called cobpoints (Heras et al. 1995), indicate the locations of the shock front
 113 which are magnetically connected to the observers. As the shock propagating outwards, the
 114 cobpoints move along the shock front towards the east. In our model, the shock front has a fixed
 115 solid angle. Note that the observer's field line is not connected to the shock front all the time. For
 116 example, the field line of the observer C is not connected to the shock at the beginning, but later,
 117 as the shock front moves to a larger radial distance than that of the observer, the field line becomes
 118 connected to the shock. Eventually, the observer will be disconnected from the shock as the shock
 119 continues to propagate outward.

120 We use boundary values to model SEP injection from the shock. The boundary condition is

121 chosen to have the following form (Kallenrode & Wibberenz 1993, 1997; Kallenrode 2001)

$$f_b(r, \theta, \varphi, p, t) = a \cdot \delta(r - v_s t) \cdot S(r, \theta, \varphi, p) \cdot p^{-\gamma} \cdot \xi(\theta, \varphi), \quad (9)$$

122 where $S(r, \theta, \varphi, p)$ is the shock efficiency

$$S(r, \theta, \varphi, p) = \left(\frac{r}{r_c}\right)^{\alpha(p)} \cdot \exp\left[-\frac{|\phi(\theta, \varphi)|}{\phi_c(p)}\right], \quad (10)$$

123 and $\xi(\theta, \varphi)$ indicates the spatial scale of the shock front

$$\xi(\theta, \varphi) = \begin{cases} 1 & \text{if } |\phi(\theta, \varphi)| \leq \phi_s \\ 0 & \text{otherwise.} \end{cases} \quad (11)$$

124 where the shock radial distance $r = r_0 + r_s$, r_0 is the inner boundary, $r_c = 1$ AU, $\alpha(p)$ controls the
 125 variation of particle injection efficiency as a function of radial distance, ϕ is the angle between
 126 shock nose and any point at the shock front where the particles are injected, ϕ_c describes how fast
 127 the shock efficiency decreases toward the flanks of the shock, and ϕ_s is the half angular width of
 128 the shock. Particles injected at the shock have an isotropic distribution.

129 We use a time-backward Markov stochastic process method to solve the transport equation
 130 (1) (Zhang 1999). The initial-boundary value problem of SEP transport equation can be
 131 reformulated with a set of stochastic differential equations, so it can be solved by a Monte-Carlo
 132 simulation of Markov stochastic process, and the SEP distribution function can be derived. In
 133 the simulation, shock is divided into a series of shells positioned at $r = r_0 + (n + 0.5)\Delta r$ in the
 134 time range $[n\Delta t, (n + 1)\Delta t)$, with $\Delta t = \Delta r/v_s$, and $n = 0, 1, 2, \dots, n_0$. Here, we set the distance
 135 between adjacent shells Δr small enough, i.e., $\Delta r = 3 \times 10^{-4}AU$, to make the discrete effects of
 136 shells negligible. For every shock shell, we trace particles from the observation time back to the
 137 initial time of source particle injection. Only those particles in the source region at the initial
 138 time contribute to the statistics. For detailed description of the method, please refer to Qin et al.
 139 (2006). In this paper, the shell model is similar to a series of onion shells which are the region
 140 swept by the shock (Zank et al. 2000). Because there is no reliable theory for the calculation of

141 particle injection at the shock, we choose this shell model with an assumed particle injection to
142 model the effect of particle acceleration by the CME shock. We also neglect the effect of strong
143 scattering by enhanced waves in the vicinity of the shock. After particles are released, they will
144 not be reaccelerated even when they encounter the shock at a later time.

145

3. Results

146 The parameters used are listed in table 1 unless otherwise stated in the text. Note that the
147 interplanetary field is the Parker field. In addition, the ratio of the perpendicular mean free path to
148 the parallel one at 1 AU is 0.0125. The perpendicular mean free path depends on the momentum
149 of particle and local magnetic field strength as described in the Equation 7.

150

3.1. Constant shock efficiency

151 Figure 2 shows our simulation results of the omnidirectional flux and anisotropy for 5 MeV
152 protons in models with and without perpendicular diffusion. The left and right panels indicate the
153 cases with and without adiabatic cooling, respectively. The shock width is 360° , and the shock
154 efficiency S is set to be a constant ($\alpha = 0, \phi_c = \infty$). The vertical dashed line indicates the moment
155 when the shock passes the observer at 1 AU.

156 From Figure 2, we can see that, in all of the panels, the results with and without perpendicular
157 diffusion are almost the same. This is because of the spherical symmetry of the SEP source.
158 Comparing the left and right panels, we can find that the adiabatic cooling effect makes a
159 significant difference in the time profiles of SEP fluxes. When there is no adiabatic cooling (left
160 panels), the fluxes rise all the time. Since the shock always releases energetic particles, the number
161 of particles in interplanetary space increases with the time. However, when there is adiabatic
162 cooling (right panels), the fluxes decrease after the shock passage of the observer. Because of

163 the adiabatic cooling effect, the observed particles at 1 AU have less energies than when they
164 were injected at the source. Since the SEP source has a negative energy spectral index, lower flux
165 would be observed for particles at the same energy at a later time.

166 It is also interesting to study the anisotropy of particle flux. Before the shock reaches the
167 observer, particles are released from the shock at distances $r < 1$ AU so that the anisotropy is
168 always positive. At the shock passage of the observer, the anisotropy suddenly jumps to zero,
169 because the injected energetic particles are set to be isotropic in the source region. After the
170 passage of the shock, the anisotropy with and without adiabatic cooling behaves differently.
171 Without the adiabatic cooling effect, the anisotropy remains near zero. However, with adiabatic
172 cooling effect, the anisotropy keeps a small negative value. Generally, the particles originated
173 from injections at $r < 1$ AU have experienced more adiabatic energy loss, so their contribution to
174 the observed particle flux is smaller than those originated from injections at $r > 1$ AU. As a result,
175 the anisotropy has a negative value. Since the adiabatic cooling is an important effect, we include
176 it in all of the following simulations.

177 Figure 3 shows the simulation results with shock efficiency S as a constant ($\alpha = 0, \phi_c = \infty$).
178 The observer is located at 1 AU equator and 0° longitude. The propagation direction of the shock
179 is indicated by the direction of shock nose. In the top six panels, the shock noses all locate in the
180 equatorial plane, but point to different longitudes. The labels E20, CM(Center Meridian), and
181 W20 indicate that the shock nose points to 20° east, 0° , and 20° west, respectively, all relative to
182 the observer. In the last two panels, the longitudes of the shock noses are all set at 0° , but their
183 latitudes are different, i.e., 20° North (N20) and 40° North (N40) from the equator. The shock
184 nose directions relative to the observer are similarly named in the rest of the paper. The vertical
185 dashed line indicates the moment of the shock passage of 1 AU, but it does not ensure the shocks
186 pass the observer because of the limited size of shock width. In the following, if the shock actually
187 passes the observer at 1 AU, the case is recorded as “the shock passage of the observer”, otherwise

188 it is recorded as “the shock passage of 1 AU”. The time interval between the two short vertical
189 solid lines indicates the time period during which the observer is connected to the shock by the
190 IMF. Note that since the enhanced turbulence and local particle acceleration at the shock are not
191 included in the model, a spike in the particle flux is absent at the shock passage of the observer.

192 Figure 3(a) and (b) show the results for events W70 and W40, respectively. We can refer
193 these events as the Western events. In the beginning, there is no obvious difference with and
194 without perpendicular diffusion, because the observer’s field line is connected to the shock since
195 the onset time in each event. The shock is not detected by the observer when passing 1 AU. After
196 the observer’s field line is disconnected from the shock, the flux starts to decay. However, the
197 flux decays more slowly with perpendicular diffusion, because after the shock is disconnected
198 from the field line, ‘new’ particles can be continuously injected to the observer’s field line through
199 perpendicular diffusion. In addition, the anisotropy is larger than zero at the beginning, and then
200 gradually decreases to zero as the shock propagates outward. During the entire events, the time
201 profiles of SEP anisotropy are almost the same with and without perpendicular diffusion.

202 Figure 3(c), (d), and (e) show results for events W20, CM, and E20, respectively. We can
203 approximately refer these events as center meridional (CM) events. For the CM events, the
204 observer’s field line is not connected to the shock at the onset time. With perpendicular diffusion,
205 SEP event starts earlier. In each event, the peak of flux appears at the shock passage of the
206 observer. After the observer’s field line is disconnected from the shock, the flux decays more
207 quickly without perpendicular diffusion.

208 Figure 3(f) shows the results for the event E40 which is referred to as Eastern events. Noted
209 that the observer’s field line is not connected to the shock until the shock passage of 1 AU. Without
210 perpendicular diffusion, the anisotropy is significantly less than zero at the beginning, which
211 means most of particles are moving towards the Sun at that time. However, with perpendicular
212 diffusion, the observed particles are nearly isotropic.

213 Figure 3(g) shows the results for the event N20, in which the SEP flux and anisotropy have
214 behaviors similar to those in the CM events, i.e., the flux peak appears at the shock passage of
215 the observer. In the event N40 shown in the Figure 3(h), the time profiles of flux and anisotropy
216 behave differently from that in the event N20. In the event N40, the observer's field line is not
217 connected to the shock at all the time, so the observer can only detect the particles coming through
218 the perpendicular diffusion. The anisotropy is always approximately equal to zero, and the flux
219 peak appears after the shock passage of 1 AU.

220 3.2. Variable shock efficiency

221 Figure 4 shows the fluxes of 5 MeV protons with different source efficiency power indexes (
222 0, -1 , -2 , and -3), which controls how fast the shock efficiency changes as a power law function
223 of the radial distance.

224 In the panels (a), (b), (c), and (d) of Figure 4, the shocks are in the direction of W70. It is
225 shown that in 4(a), when the source efficiency is a constant, the flux decreases more slowly with
226 perpendicular diffusion. As the shock efficiency decreasing in the panels from (a) to (c), the fluxes
227 with perpendicular diffusion decrease more and more quickly, and the difference in fluxes between
228 the cases with and without perpendicular diffusion becomes smaller and smaller. Especially, in
229 Figure 4(d), when the index is -3 , the flux with perpendicular diffusion becomes even smaller
230 than that without perpendicular diffusion. It is known that with perpendicular diffusion two kinds
231 of processes are in operation: the gain of particles arriving at the observer's field line from nearby
232 field lines, and the loss of particles from the observer's field line. The gain (or loss) of particles
233 with the perpendicular diffusion can make the flux decrease more slowly (or quickly) in the
234 decay phase than without the perpendicular diffusion. In addition, the power index of the shock
235 efficiency mainly influences the gains of particles. As the shock efficiency power index decreases
236 from 0 to -3 , particles arriving at the observation point by crossing field lines at a later time

237 become less important. In Figure 4(d), the gain of particles is too slow to compensate the loss of
238 particles, so the flux without the perpendicular diffusion is larger than that with the perpendicular
239 diffusion. In the panels (e), (f), (g) and (h) of Figure 4 the shocks propagate in the CM direction,
240 and in the panels (i), (j), (k), and (l) of Figure 4 the shocks head towards E40. Comparing with the
241 case W70, we can see a similar behavior in the decay phases of fluxes in the cases of CM and E40.

242 Figure 5 shows the results of simulations similar to that shown in Figure 3. The only difference
243 is that now the shock efficiency S changes as a power law function of the radial distance times
244 an exponential function of the angle distance from the shock nose, $S \sim (r/r_c)^{-2} \exp(-|\phi|/15^\circ)$. In
245 addition, the y-title ‘E’ in each panel shows the time evolution of the shock’s logarithm efficiency
246 at the cobpoint ($E \equiv \log S$). Although the flux is not just affected by strength of boundary
247 condition at the current time, the cobpoint efficiency is still very important, because the speed of
248 particles is much faster than that of shock and the parallel diffusion coefficient is larger than the
249 perpendicular one.

250 In the events W70 and W40 shown in Figure 5(a) and (b), respectively, the shock efficiency at
251 the cobpoint decreases with time very quickly, so the peaks of fluxes appear earlier than the cases
252 with a constant shock efficiency (Figure 3(a) and (b)). In the event W70, the observer’s field line
253 is disconnected from the shock very early, so there are only a small number of particles arriving
254 at the observation point directly from the source following the field lines. With the perpendicular
255 diffusion, the flux decreases more slowly than that without the perpendicular diffusion. However,
256 in the event W40 shown in Figure 5(b), after the observer’s field line is disconnected from the
257 shock, the flux decays more quickly with the perpendicular diffusion than without it. Since the
258 observer’s field line is connected to the shock for a longer time than that in the event W70, more
259 particles arrive at the observation point directly from the shock along the field line. But with the
260 perpendicular diffusion, the loss of particles in the event W40 is faster than the gain of particles.
261 Therefore the flux decreases more quickly with the perpendicular diffusion than without it. Since

262 the observer’s field line is disconnected from the shock before the shock passage of 1 AU, the
263 anisotropy gradually decreases to zero, and there is no jump at the shock passage in these events.

264 In the events W20, CM, E20, and E40 shown in Figure 5(c), (d), (e), and (f), respectively,
265 when the cobpoint reaches the shock nose, the shock efficiency reaches the maximum, and the
266 peak of flux appears in each event. After that, the fluxes gradually decay with the time. In
267 particular, for the event CM in Figure 5(d), the cobpoint reaches shock nose at 1 AU, so the peak
268 of flux appears at the shock passage of the observer. However, for the event W20 in Figure 5(c),
269 since the cobpoint reaches shock nose inside 1 AU, the peak of flux appears before the shock
270 passage of the observer. Likewise, for the events E20 and E40 in Figures 5(e) and (f), respectively,
271 the flux peaks appear after the shocks passage for similar reasons. In the event N20 shown in
272 Figure 5(g), the flux and anisotropy behave similarly to those shown in the event CM. However,
273 for the event N40 shown in Figure 5(h), the observer’s field line is not connected to the shock all
274 the time and the cobpoint does not exist anymore. So the observer can only detect the particles
275 coming through the perpendicular diffusion.

276 Figure 6 shows the simulations of 5 MeV proton with different perpendicular diffusion
277 coefficients. The perpendicular mean free path is set to $\lambda_{\perp} = 0.0025$ AU and $\lambda_{\perp} = 0.025$ AU,
278 where radial mean free path is $\lambda_r = 0.1$ AU ($\lambda_{\parallel} \approx 0.2$ AU at 1 AU). With the larger perpendicular
279 mean free path, the onset time of flux moves to an earlier time. In each of the E20 and E40 events,
280 the peak time of flux comes earlier with the stronger perpendicular diffusion. Furthermore, with
281 the stronger perpendicular diffusion, the peak intensity of flux is less than that with the weaker
282 perpendicular diffusion in all the events, except the N40 event. In the N40 event, all the particles
283 arrive at the observation point by crossing field lines, so the flux should be larger with the stronger
284 perpendicular diffusion. Anisotropy in the N40 event is always near zero. It is also noted that there
285 is no significant difference in the anisotropy with different perpendicular diffusion coefficients in
286 all the events shown in this figure.

4. Summary

287

288 In our model, we assume the ICME shock as a moving source of SEPs with varying strength
289 as a function of location and time, as it propagates through the Parker IMF. We investigate how
290 the injected particles transport with varying conditions of shock geometry and mean free paths.
291 Our SEP transport equation essentially includes all necessary particle transport mechanisms,
292 such as particle streaming along field line, magnetic focusing in the diverging IMF, adiabatic
293 deceleration in the expanding solar wind, and the diffusion parallel and perpendicular to the IMF.
294 However, comparing with previous works (e.g., Zank et al. 2000; Ng et al. 2003; Sokolov et al.
295 2004), we neglected a few mechanisms, for example, particle acceleration by the CME shock,
296 wave generation by the streaming particles, and realistic geometry of the CME shock. Since the
297 prediction of SEP flux requires a precise mechanism for particle injection into the diffusive shock
298 acceleration, which is currently not available, we have adopted a diffusion model to describe
299 some general effects of particle transport processes. In this paper, we have studied the effects
300 of perpendicular diffusion on 5 MeV protons produced by the ICME shock by numerically
301 solving the focused Fokker-Planck transport equation of energetic particles. We have shown the
302 time profiles of particle flux and anisotropy as observed at 1 AU in the cases with and without
303 perpendicular diffusion. Our new findings are listed as follows.

304 (1) The adiabatic cooling plays an important role in the transport of SEPs. The adiabatic
305 cooling can cause SEPs to become less energetic while transporting in the heliosphere, so that
306 the SEPs with the same energy observed later are generally originated with higher energies at the
307 source. Because the source has a negative energy spectral index, the flux decreases more quickly
308 with adiabatic cooling than without it. The SEP flux decay rate and anisotropy are affected by the
309 adiabatic cooling effect and the spectral index of the source particles.

310 (2) With the perpendicular diffusion, particles can be detected before the observer is connected
311 to the shock by field lines, and the particles detected at the onset time have experienced significant

312 perpendicular diffusion. Therefore, the anisotropy is smaller with the perpendicular diffusion at
313 the onset than without it. Since the SEP source is assumed isotropic and particles can cross the
314 shock freely in our model, the anisotropy can jump to zero or even a negative value at the shock
315 passage of the observer. No obvious difference is seen in the anisotropy with and without the
316 perpendicular diffusion, except in the onset time of field line connection to the shock.

317 (3) With the perpendicular diffusion, two kinds of processes are in operation, the gain of
318 particles from other field lines to the observer's field line, and the loss of particles by leaving the
319 observer's field line. The gains (or losses) of particles can make the flux decrease more slowly (or
320 quickly) in the decay phase than without the perpendicular diffusion.

321 (4) When the shock efficiency is a constant, the time profile of SEP flux is significantly
322 influenced by the shock position. After the observer's field line is disconnected from the shock,
323 the flux begins to decay with the time. With the perpendicular diffusion, the gain of particles is
324 faster than the loss of particles, so the flux decreases more slowly than without it.

325 (5) When the shock efficiency changes with a power law function of the radial distance, the
326 time profile of SEP flux is influenced by both the shock efficiency and shock position. When the
327 shock efficiency is a constant, the flux decreases more slowly with the perpendicular diffusion than
328 without it. However, as the shock efficiency decreases, the loss of particles becomes increasingly
329 significant relative to the gain, and the difference in the fluxes with and without the perpendicular
330 diffusion gets smaller. Especially, when the power index is small enough, a quick decrease of the
331 shock efficiency can make the flux decrease more quickly with the perpendicular diffusion.

332 (6) When the shock efficiency varies with a power law function of the radial distance and an
333 exponential law in the angular distance from the shock nose, $S \sim (r/r_c)^{-2} \exp(-|\phi|/15^\circ)$, the flux
334 peaks when the cobpoint reaches the shock nose. In addition, with a larger perpendicular mean
335 free path, the onset time of flux is earlier, and the peak intensity is lower, except for the case in
336 which the observer's field line is not connected to the shock all the time. In the case which has no

337 direct connection to the shock, all particles reach the observation point by crossing the field lines,
338 so the peak intensity is higher with a larger perpendicular mean free path.

339 In future works, we will extend our model to study particle acceleration by CME shocks. We
340 intend to include a realistic three-dimensional CME shock, local wave generated by streaming
341 particles, and diffusion coefficients derived from some advanced theories of particle transport
342 (e.g., NLGC theory, Matthaeus et al. 2003). In this way, more physical mechanisms in the gradual
343 SEP events can be studied.

344 The authors thank an unknown referee for the valuable comments. This research work
345 was partly supported by grants NNSFC 41125016, NNSFC 40921063, NNSFC 41074125,
346 CMA grant GYHY201106011, and National High-tech R&D Program of China (863 Program)
347 2010AA122200. The computations were performed by Numerical Forecast Modeling R&D and
348 VR System of State Key Laboratory of Space Weather and Special HPC work stand of Chinese
349 Meridian Project. MZ was supported in part by NASA Grants NNX08AP91G, NNX09AG29G
350 and NNX09AB24G.

REFERENCES

351

352 Beeck, J., & Wibberenz, G. 1986, ApJ, 311, 437

353 Bieber, J. W., Matthaeus, W. H., Smith, C. W., Wanner, W., Kallenrode, M.-B., & Wibberenz, G.

354 1994, ApJ, 420, 294

355 Bieber, J. W., Matthaeus, W. H., Shalchi, A., & Qin, G. 2004, Geophys. Res. Lett., 31, 10, L10805

356 Cane, H. V., Reames, D. V., & von Rosenvinge, T. T. 1988, J. Geophys. Res., 93, 9555

357 Dwyer, J. R., Mason, G. M., Mazur, J. E., Jokipii, J. R., von Rosenvinge, T. T., & Lepping, R. P.

358 1997, ApJ, 490, L115

359 Earl, J. A. 1974, ApJ, 193, 231

360 Gordon, B. E., Lee, M. A., Möbius, E., & Trattner, K. J. 1999, J. Geophys. Res., 104, 28263

361 Hasselmann, K., & Wibberenz, G. 1968, Z. Geophys., 34, 353

362 He, H.-Q., Qin, G., & Zhang, M. 2011, ApJ, 734, 74

363 Heras, A. M., Sanahuja, B., Lario, D., Smith, Z. K., Detman, T., & Dryer, M. 1995, ApJ, 445, 497

364 Heras, A. M., Sanahuja, B., Smith, Z. K., Detman, T., & Dryer, M. 1992, ApJ, 391, 359

365 Isenberg, P. A. 1997, J. Geophys. Res., 102, 4719

366 Jokipii, J. R. 1966, ApJ, 146, 480

367 Kallenrode, M. 2001, J. Geophys. Res., 106, 24989

368 Kallenrode, M., & Wibberenz, G. 1993, Int. Cosmic Ray conf., Vol. 3, 298

369 Kallenrode, M., & Wibberenz, G. 1997, J. Geophys. Res., 102, 22311

- 370 Kota, J., & Jokipii, J. R. 1995, *Science*, 268, 1024
- 371 Lario, D., Sanahuja, B., & Heras, A. M. 1998, *ApJ*, 509, 415
- 372 Lee, M. A. 1983, *J. Geophys. Res.*, 88, 6109
- 373 —. 2005, *ApJS*, 158, 38
- 374 Li, G., Zank, G. P., & Rice, W. K. M. 2003, *J. Geophys. Res.*, 108, 1082
- 375 Liu, Y., Luhmann, J. G., Bale, S. D., & Lin, R. P. 2011, *ApJ*, 734, 84
- 376 Matthaeus, W. H., Qin, G., Bieber, J. W., & Zank, G. P. 2003, *ApJ*, 590, L53
- 377 Ng, C., Reames, D., & Tylka, A. 1999, *Geophys. Res. Lett.*, 26, 2145
- 378 Ng, C., Reames, D., & Tylka, A. 2001, in *Int. Cosmic Ray conf.*, Vol. 8, 3140
- 379 Ng, C., Reames, D., & Tylka, A. 2003, *ApJ*, 591, 461
- 380 Qin, G. 2002, PhD thesis, UNIVERSITY OF DELAWARE
- 381 —. 2007, *ApJ*, 656, 217
- 382 Qin, G. & Shalchi, A. 2009, *ApJ*, 707, 61
- 383 Qin, G., Matthaeus, W. H., & Bieber, J. W. 2002, *Geophys. Res. Lett.*, 29(4), 1048
- 384 Qin, G., Matthaeus, W. H., & Bieber, J. W. 2002, *ApJ*, 578, L117
- 385 Qin, G., Zhang, M., & Dwyer, J. R. 2006, *J. Geophys. Res.*, 111, 8101
- 386 Qin, G., Zhang, M., Dwyer, J. R., & Rassoul, H. K. 2004, *ApJ*, 609, 1076
- 387 Qin, G., He, H.-Q., & Zhang, M. 2011, *ApJ*, 738, 28
- 388 Reames, D. V. 1999, *Space Sci. Rev.*, 90, 413

- 389 Rice, W. K. M., Zank, G. P., & Li, G. 2003, *J. Geophys. Res.*, 108, 1369
- 390 Roelof, E. C. 1969, in *Lectures in High-Energy Astrophysics*, ed. H. Ögelman & J. R. Wayland,
391 NASA SP- 199, 111, 1969
- 392 Schlickeiser, R. 2002, *Cosmic Ray Astrophysics*, ed. Schlickeiser, R.
- 393 Shalchi, A., Bieber, J. W., Matthaeus, W. H., & Qin, G. 2004, *ApJ*, 616, 617
- 394 Skilling, J. 1971, *ApJ*, 170, 265
- 395 Sokolov, I., Roussev, I., Gombosi, T., Lee, M., Kóta, J., Forbes, T., Manchester, W., & Sakai, J.
396 2004, *ApJ*, 616, L171
- 397 Wiedenbeck, M. E., et al. 2010, *AIP Conf. Proc.*, 1216, 621
- 398 Zank, G. P., Rice, W. K. M., & Wu, C. C. 2000, *J. Geophys. Res.*, 105, 25079
- 399 Zank, G., Li, G., Florinski, V., Hu, Q., Lario, D., & Smith, C. 2006, *J. Geophys. Res.*, 111, A06108
- 400 Zhang, M. 1999, *ApJ*, 513, 409
- 401 —. 2006, *J. Geophys. Res.*, 111, 4208
- 402 Zhang, M., Jokipii, J. R., & McKibben, R. B. 2003, *ApJ*, 595, 493
- 403 Zhang, M., Qin, G., & Rassoul, H. 2009, *ApJ*, 692, 109

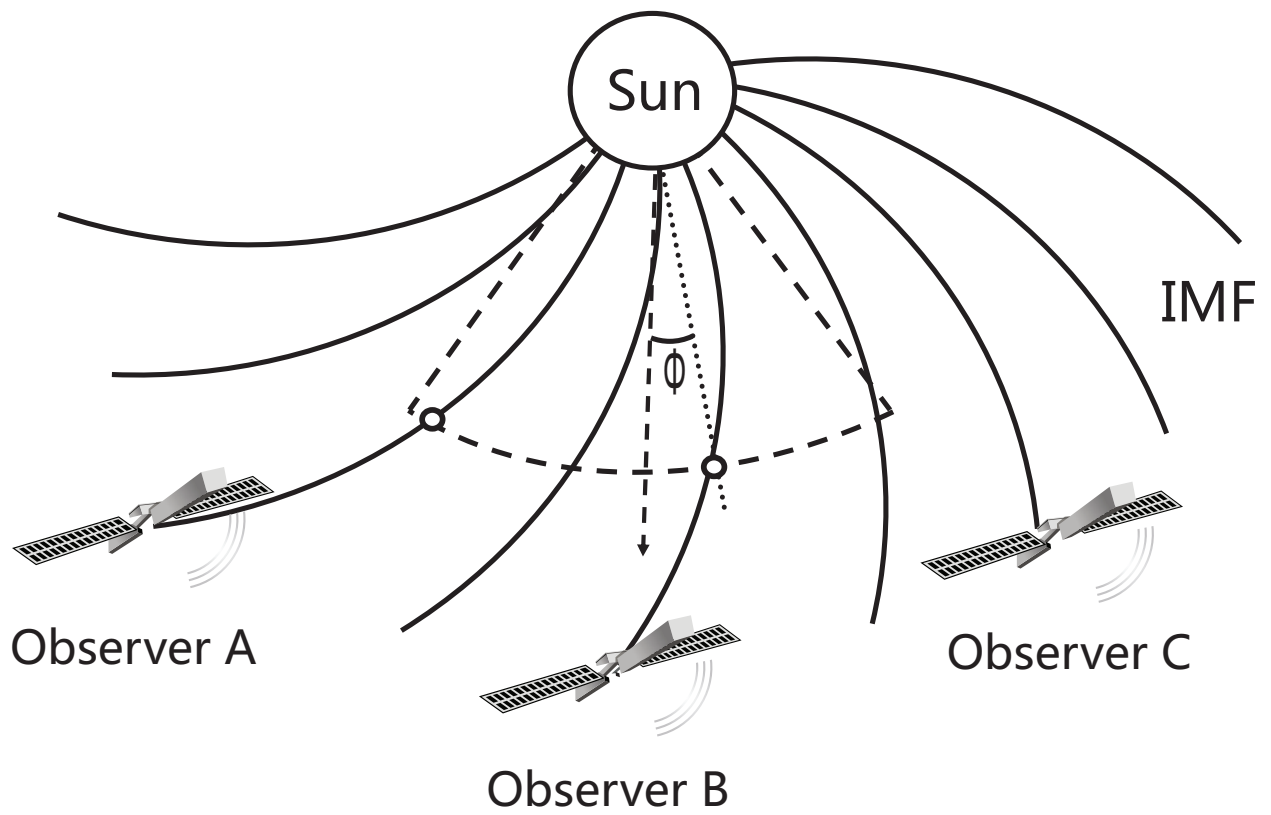


Fig. 1.— Geometry of a CME shock cross section with three observers at different locations. The dashed arrow radial line indicates the shock nose. The two circles represent the two cobpoints.

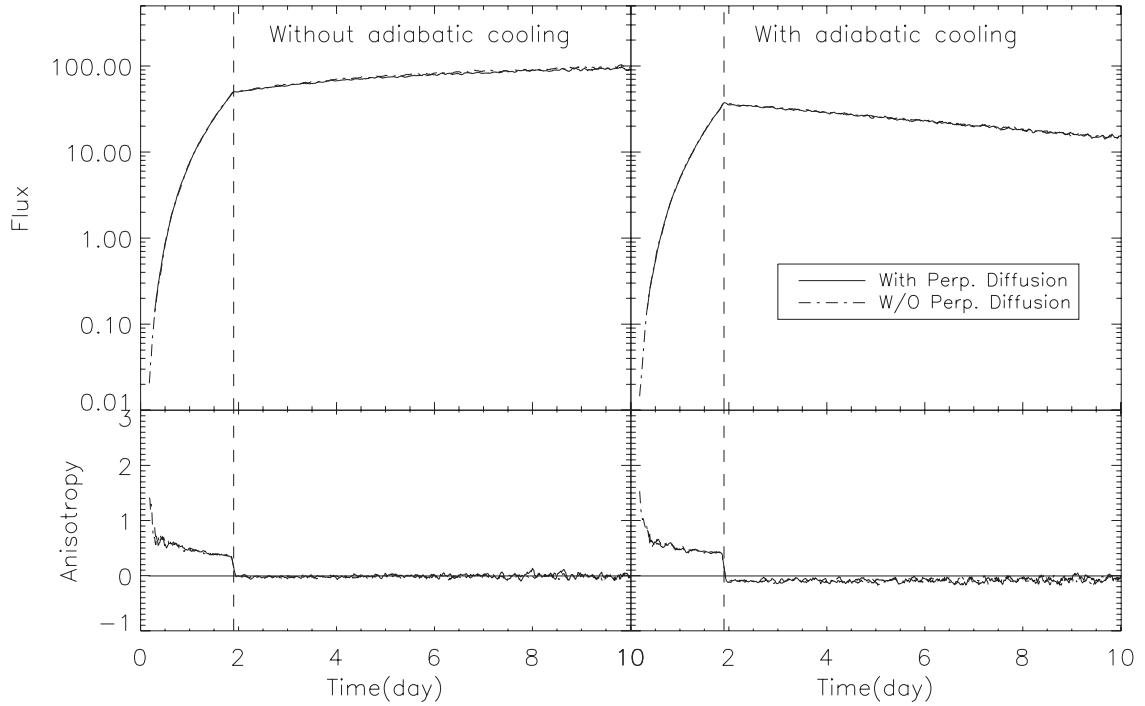


Fig. 2.— Comparison of 5 MeV protons flux and anisotropy with perpendicular diffusion (solid line) and without perpendicular diffusion (dash-dotted line). The left and right panels show the results without and with adiabatic cooling effects, respectively. The shock width is 360° and the shock efficiency is a constant. The vertical dashed line indicates the moment when the shock passes the observer at 1 AU in each panel.

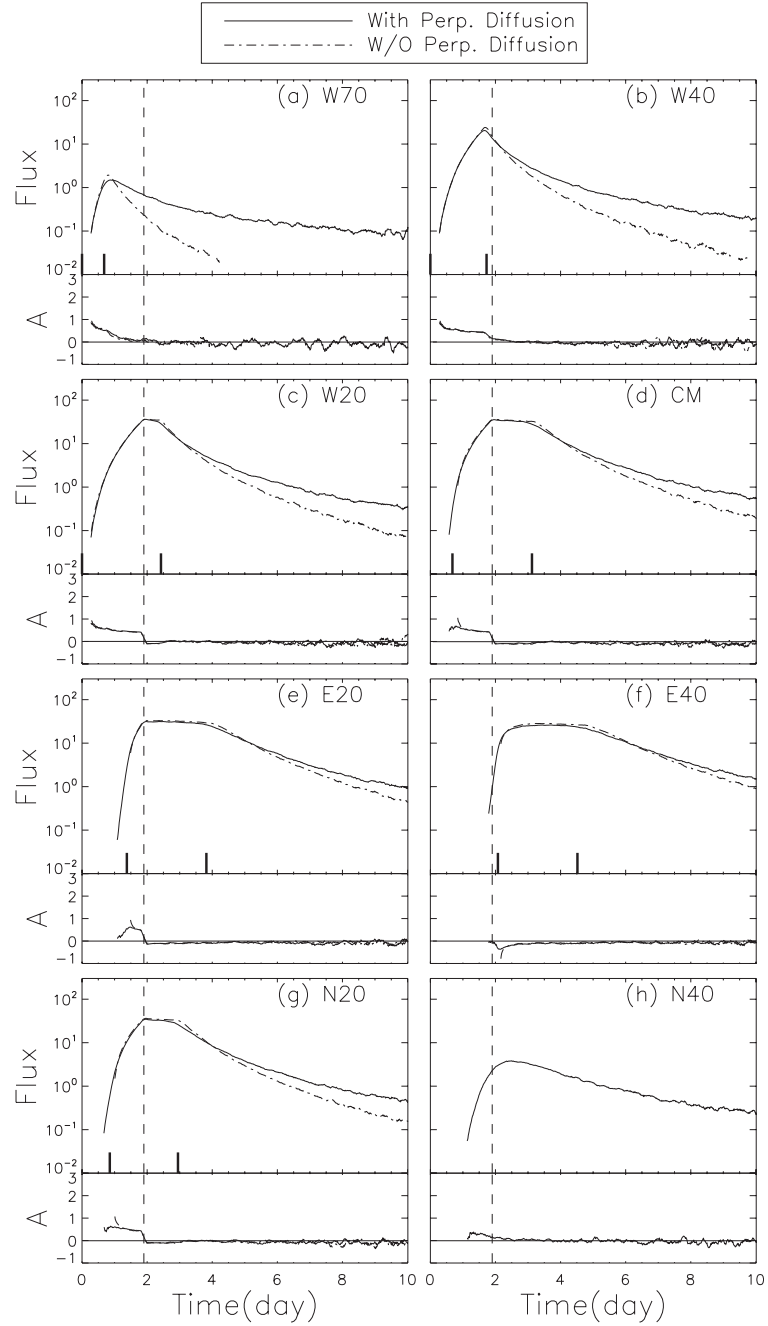


Fig. 3.— Comparison of 5 MeV protons flux and anisotropy with perpendicular diffusion (solid lines) and without perpendicular diffusion (dash-dotted lines). The shock width is 70° and the shock efficiency is a constant. The vertical dashed line indicates the moment of the shock passage. The time interval between the two short vertical solid lines indicates the time during which the observer’s field line is connected to the shock. Different sub-figure indicates different shock nose directions relative to the observer.

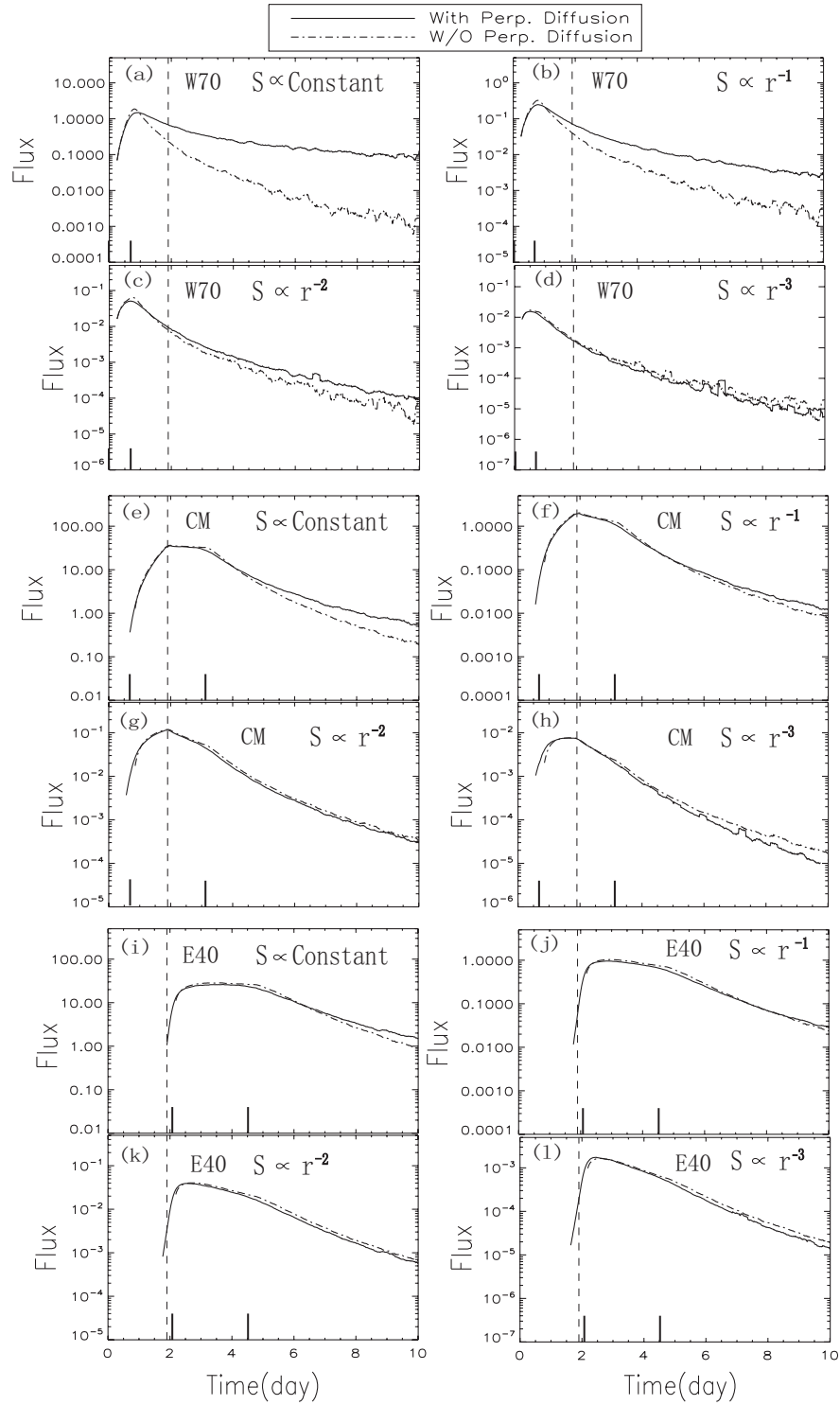


Fig. 4.— Comparison of 5 MeV proton fluxes in the cases of different power indices of shock efficiency.

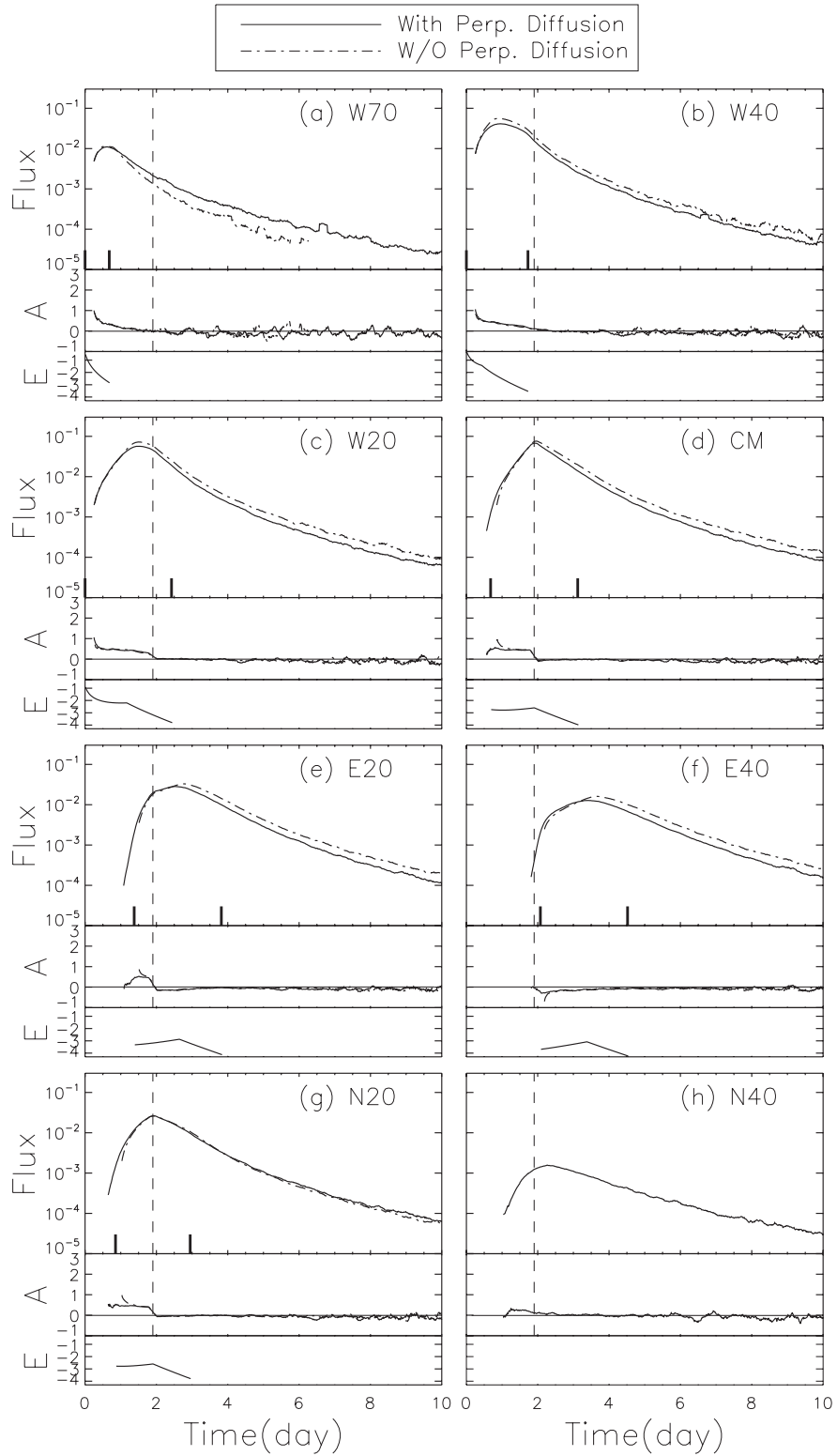


Fig. 5.— Same as Figure 3 except that the shocks’ efficiency changes with a power law in radial distance and an exponential law in angle distance from the shock nose, $S \sim (r/r_c)^{-2} \exp(-|\phi|/15^\circ)$, and that an additional panel showing the time profile of cobpoint efficiency $E = \log(S)$ is added for each sub-figure.

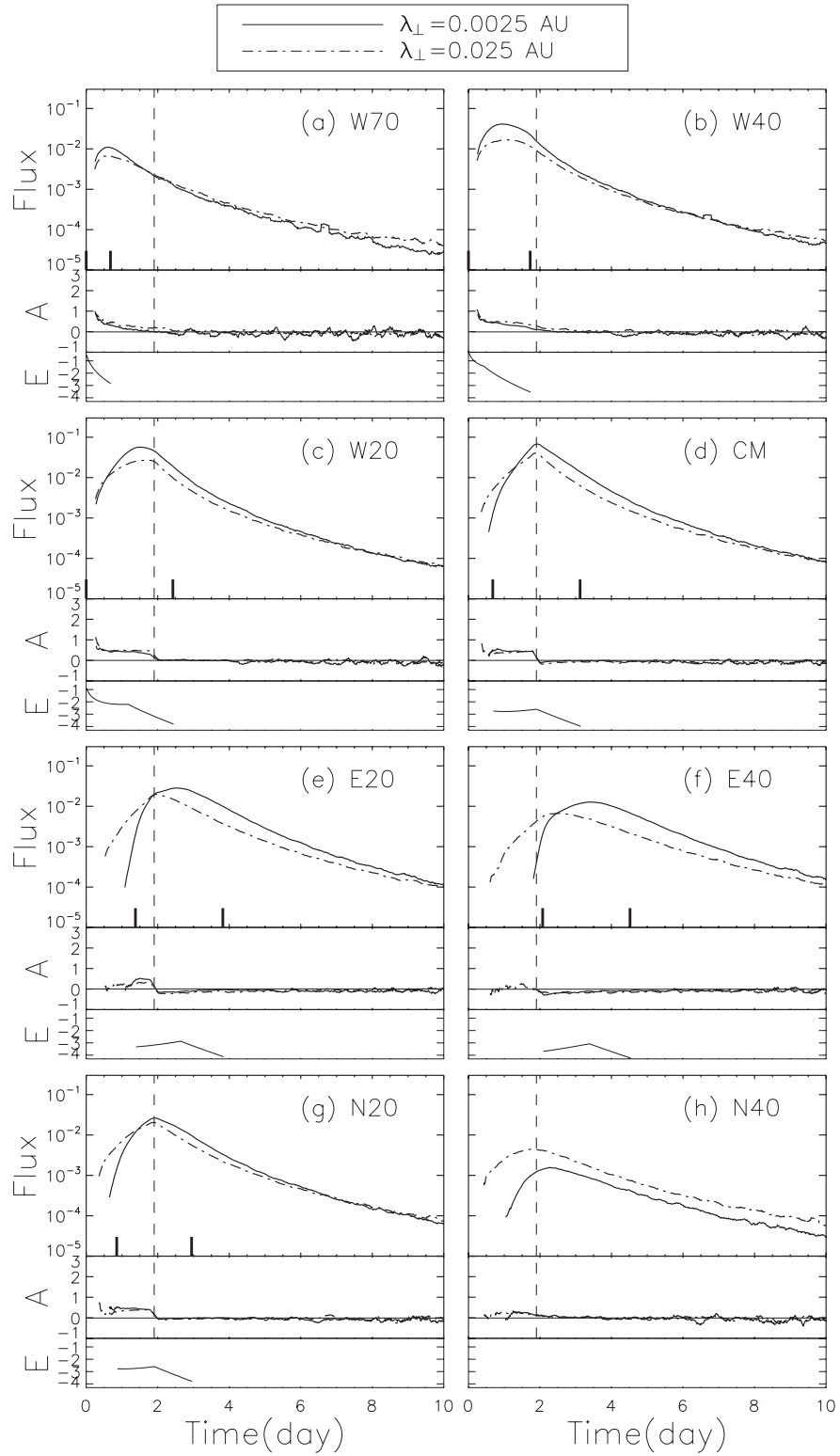


Fig. 6.— Same as Figure 5 except that different line styles indicate different perpendicular mean free paths.

Table 1: Model Parameters Used in the Calculations.

Parameter	Physical meaning	Value
V^{sw}	solar wind speed	400 km/s
v_s	shock speed	870 km/s
ϕ_s	shock width	35°
r_O	observer solar distance	1 AU
θ_O	observer latitude	90°
ϕ_O	observer longitude	0°
γ	injection spectrum	–5.5
E	particles energy	5 MeV
λ_r	particle radial mean free path	0.1 AU ^a
λ_{\perp}	particle perpendicular mean free path	0.0025 AU ^b
r_{b0}	inner boundary	0.05 AU
r_{b1}	outer boundary	50 AU
r_c	solar distance unit	1 AU

^aFor 5 MeV particles throughout heliosphere.

^bFor 5 MeV particles at 1 AU.